J Mater Sci (2022) 57:8634–8647

Ceramics

Enhanced red emission in $Sr_{(1-x)}Eu_xMo_{0.5}W_{0.5}O_4$ (x = 0.01, 0.02, 0.04) phosphor and spectroscopic analysis for display applications

L. X. Lovisa[1,*], D. F. Dos Santos[2], A. A. G. Santiago[2], M. Siu Li[3], E. Longo[4], F. V. Motta[2], and M. R. D. Bomio[2]

[1] Institute of Physics and Chemistry, Federal University of Itajubá (UNIFEI), Itajubá, MG 37500-903, Brazil
[2] LSQM–Laboratory of Chemical Synthesis of Materials–Department of Materials Engineering, Federal University of Rio Grande Do Norte, P.O. Box 1524, Natal, RN 59078-900, Brazil
[3] IFSC, USP, Av. Trabalhador São Carlense, 400, CEP, São Carlos, SP 13566-590, Brazil
[4] CDMF-LIEC, UFSCar, P.O. Box 676, São Carlos, SP 13565-905, Brazil

Received: 16 December 2021
Accepted: 5 April 2022
Published online: 27 April 2022

ABSTRACT

The particles of the solid solution of strontium molybdate and tungstate ($SrMo_{0.5}W_{0.5}O_4$) were doped with Eu^{3+} ions at concentrations of 1, 2 and 4 mol% synthesized by the microwave-hydrothermal method (MHM). The structural analyses of the particles were conducted by XRD with Rietveld Refinement and FT-Raman spectroscopy. The crystallization and growth of particles were investigated by FEG-SEM and proposed a mechanism of particle development involving the steps: nucleation and further growth. The $SrMo_{0.5}W_{0.5}O_4$ presented white emission with the chromaticity coordinates: (0.32; 0.40). The $Sr_{(1-x)}Eu_xMo_{0.5}W_{0.5}O_4$ samples exhibited an increase in luminescence intensity in the red region as the concentration of Eu^{3+} increases, a behavior attributed to the $^5D_0 \rightarrow {}^7F_2$ transition of Eu^{3+} (623 nm). The $Sr_{(1-x)}Eu_xMo_{0.5}W_{0.5}O_4$ samples showed high color purity (≈ 97%), as well as the results of the color reproduction index (CRI) reached 80% level. The radiation luminous efficiency (LER) presented by the samples exhibited values of 322 $lm.W^{-1}$. According to the quality of the photometric parameters presented, the samples have attributions for application in solid-state lighting devices.

Handling Editor: David Cann.

Address correspondence to E-mail: lauraengmat@hotmail.com

https://doi.org/10.1007/s10853-022-07203-x

GRAPHICAL ABSTRACT

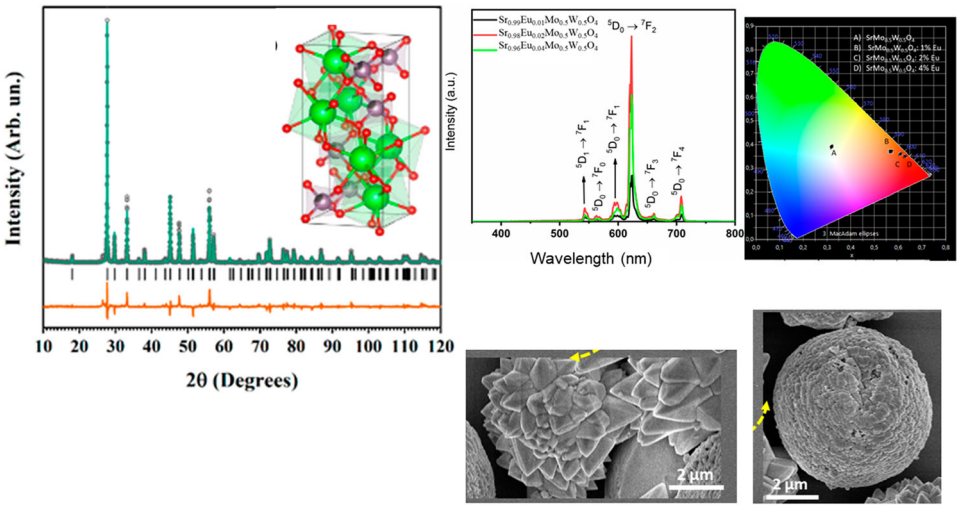

Introduction

Inorganic materials doped with rare earth ions have become essential to develop devices and advanced optical technologies to generate light [1]. Due to their optical, electronic and chemical properties, these materials play a fundamental role as high-performance luminescent equipment in modern lighting and display devices, as well as phosphors, light-emitting diodes (LEDs), laser hosts, emissive screens, heat-resistant materials, humidity sensors, fluorescent lamps, optical data storage, and catalysts, among other applications [2–5].

Metal molybdates have been successfully used as rare earth host matrices for luminescent materials because of their excellent physical and chemical properties [6–9]. In particular, $SrWO_4$ and $SrMoO_4$ have been considered the most efficient host matrices for various types of rare earth ions, such as Yb^{3+}/Er^{3+}, Eu^{3+}, Gd^{3+}, Pr^{3+}, Ho^{3+}, Sm^{3+} and Nd^{3+} [10–12].

The direct excitation of Eu^{3+} ions is considered to be an inefficient process because of the prohibited nature of the 4f transitions. However, these ions are responsible for exhibiting efficient luminescence through UV excitation when they are inserted into inorganic materials. Eu^{3+} has intense and narrow emission lines that go from red to near infrared when excited by UV wavelength, which leads it to often being used as a doping element [13]. According to Gai et al. [14], these materials have several advantages attributed to the shielding of the 4f electrons, such as large Stokes shift, sharp emission spectrum, long lifetime, high chemical/photochemical stability, low toxicity and reduced photobleaching. The Eu^{3+} concentration used in the matrix provides maximum PL intensity especially that associated with the transition $^5D_0 \rightarrow {}^7F_2$. It is crucial to assess the influence of Eu^{3+} on the structural, optical and morphological behavior of materials.

Although many works have focused their attention on studying molybdate and tungstate phosphors separately, only a few have been developed with mixed inorganic molybdate-tungstate phosphors doped with lanthanides. Thus, this article presents an approach on the synthesis of $Sr_{(1-x)}Eu_xMo_{0.5}W_{0.5}O_4$ and its characterization, as well as a study of its structural, vibrational, morphological and photoluminescent properties.

Experimental

Materials

Sodium molybdenum oxide dihydrate ($Na_2MoO_4 \bullet 2H_2O$, 98%, Alfa Aesar), sodium tungsten oxide dihydrate ($Na_2WO_4 \bullet 2H_2O$, 95%, Alfa Aesar), calcium nitrate ($Ca(NO_3)_2 \bullet 4H_2O$, 99%, Alfa Aesar),

europium oxide (Eu_2O_3, 99%, Aldrich), nitric acid (HNO_3, 65%, Synth), ammonium hydroxide (NH_4OH, 24%, Synth) and distilled water were used as received to prepare the $SrMo_{0.5}W_{0.5}O_4$ and $Sr_{(1-x)}Eu_xMo_{0.5}W_{0.5}O_4$ particles.

Synthesis

Eu_2O_3 oxide was initially dissolved separately in 10 ml of nitric acid to obtain europium nitrate. Two precursor solutions were prepared to synthesize the $SrMo_{0.5}W_{0.5}O_4$ and $Sr_{(1-x)}Eu_xMo_{0.5}W_{0.5}O_4$ particles: one containing molybdenum (solution A) and the other containing tungsten (solution B), with a molar ratio (Mo:W) of 0.5:0.5. The starting reagent was dissolved in 40 ml of distilled water for both solutions. Solution B was added to solution A by dripping and under constant magnetic stirring. Stoichiometrically weighed strontium was subsequently added after complete dissolution. Doping with Eu^{3+} occurred at 1, 2 and 4 mol% concentrations for the $SrMo_{0.5}W_{0.5}O_4$ sample. Finally, NH_4OH was added to the solution to stabilize its pH at 8 in observing the precipitate formation. The mixture was transferred into a Teflon autoclave, which was sealed and placed into a microwave-hydrothermal system (2.45 GHz, maximum power of 800 W). The microwave-hydrothermal conditions were kept at 120 °C for 20 min with a heating rate fixed at 3 °C/min. The pressure in the autoclave was stabilized at 3.0 atm. After the microwave-hydrothermal treatment, the autoclave was cooled to room temperature. The resulting solution was washed with deionized water several times, and the white precipitates were finally collected. Using the same experimental conditions, the obtained powders were dried in a conventional furnace at 100 °C for 24 h.

Characterization

The $SrMo_{0.5}W_{0.5}O_4$ and $Sr_{(1-x)}Eu_xMo_{0.5}W_{0.5}O_4$ particles were structurally characterized by XRD using a Shimadzu XRD 7000 instrument with CuKa radiation (λ = 1.5406 Å) in the 2θ range of 10 to 80° at a scan rate of 0.02 s^{-1}. Raman spectroscopy measurements were recorded using a T-64000 triple monochromator spectrometer (Jobin–Yvon, France) coupled to a CCD detector. The spectroscopy was performed using a 514.5 nm wavelength of an argon ion laser, keeping its maximum output power at 8 mW. The morphologies were investigated using field-emission gun scanning electron microscopy (FEG-SEM) (Carl Zeiss, Supra 35- VP Model, Germany) operated at 6 kV. The UV–vis diffuse reflectance spectrum was measured at room temperature using a UV–vis spectrometer. The photoluminescence (PL) spectra were acquired with an Ash Monospec 27 monochromator (Thermal Jarrel, U.S.A.) and a R4446 photomultiplier (Hamamatsu Photonics, U.S.A.). The 325 nm beam of a krypton ion laser (Coherent Innova 90 K) was used as the excitation source with an output of approximately 13.3 mW. All measurements were performed at room temperature.

Results

XRD

Figure 1 shows a comparison of XRD standards for $SrMo_{0.5}W_{0.5}O_4$ and $Sr_{(1-x)}Eu_xMo_{0.5}W_{0.5}O_4$ samples with JCPDS No. 85–0587. It can be observed that all diffraction peaks are possibly indexed as a tetragonal structure with the *I41/a* spatial group. The hexavalent atoms (M^{6+} = Mo^{6+}, W^{6+}) are coordinated by four O^{2-} atoms, while the divalent atoms (Sr^{2+}) are coordinated by eight O^{2-} atoms [15]. Due to the approximation of the ionic rays of Mo^{6+} (0.41 Å) and W^{6+} (0.42 Å), it can be seen that the replacement of $Mo^{6+} \rightarrow W^{6+}$ occurs successfully. The (112) plane presents a displacement for smaller dispersion angles depending on the Eu^{3+} concentration.

The Sr^{2+} atoms for the $Sr_{(1-x)}Eu_xMo_{0.5}W_{0.5}O_4$ samples are replaced by Eu^{3+} atoms without major changes in the $SrMo_{0.5}W_{0.5}O_4$ lattice, since the Sr^{2+} (1.26 Å for CN = 8) and Eu^{3+} (1.07 Å for CN = 8) ionic radii are close, favoring the doping. The high amplitude diffraction peaks indicate that the synthesized $SrMo_{0.5}W_{0.5}O_4$ and $Sr_{(1-x)}Eu_xMo_{0.5}W_{0.5}O_4$ were well crystallized. No influence related to the incorporation of Eu^{3+} ions into the structure was proven. The average crystallite sizes were estimated by the Scherrer equation using the main (112) plane for the calculations.

Figure S1 of supplementary information illustrates the Rietveld refinement graph of the $SrMo_{0.5}W_{0.5}O_4$ and $Sr_{(1-x)}Eu_xMo_{0.5}W_{0.5}O_4$ samples obtained by MHM. The $SrMo_{0.5}W_{0.5}O_4$ (and $Sr_{(1-x)}Eu_xMo_{0.5}W_{0.5}O_4$) structure parameters, unit cell volume, bond length and bond angles were obtained and calculated

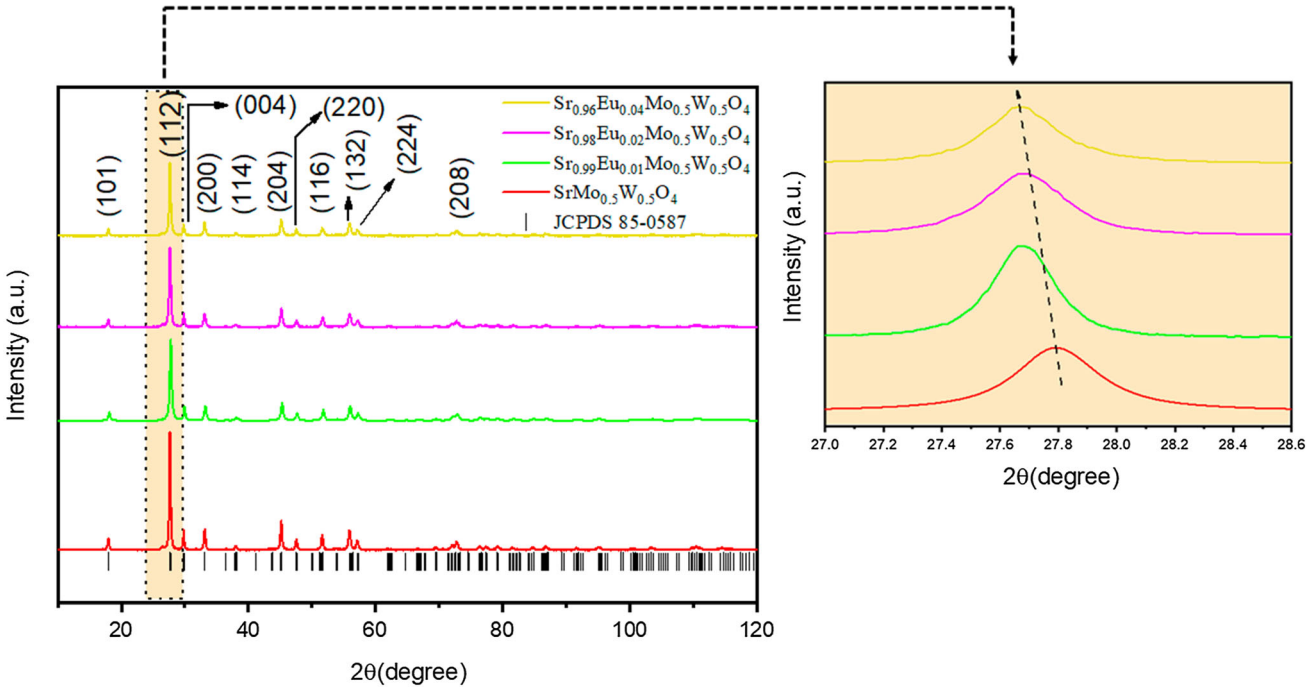

Figure 1 XRD patterns of $SrMo_{0.5}W_{0.5}O_4$ and $Sr_{(1-x)}Eu_xMo_{0.5}W_{0.5}O_4$ samples and peak displacement of the (112) plane.

by the Rietveld refinement method using the GSAS (General Structure Analysis System) program with EXPGUI graphical interface [16]. Through the Rietveld refinement analysis, it is possible to estimate an approximation of the structural model to a real structure from the powder intensity profile measurements. The result of the presented theoretical adjustment indicates good agreement with such analysis, where small differences in the intensity scale close to zero can be observed, as illustrated by the line (Exp—Calc). The lattice parameters, such as unit cell volume and crystallite size obtained through the Rietveld refinement of the $SrMo_{0.5}W_{0.5}O_4$ and $Sr_{(1-x)}Eu_xMo_{0.5}W_{0.5}O_4$ samples, as well as the quality coefficients of the refinement (R_P, Rf^2, X^2) can be found in Table 1. These parameters are listed in Table 1 and suggest that the measured diffraction patterns are in good agreement with the ICSD entry No. 99089.

Small changes in the lattice parameters associated with the substitution of $Sr^{2+} \rightarrow Eu^{3+}$ in the $SrMo_{0.5}W_{0.5}O_4$ samples. In addition, some modifications found in $Sr_{(1-x)}Eu_xMo_{0.5}W_{0.5}O_4$ samples resulted in a variation in the crystallite size and distortions of the clusters. The cell volume tended to decrease with an increase in the dopant concentration since the Eu^{3+} ionic radii became smaller than those of Sr^{2+}. The crystallite size of the samples also decreased with doping. This behavior can be explained by the fact that the increase in the percentage of Eu^{3+} cations was accompanied by an increase in the number of defects in the $SrMo_{0.5}W_{0.5}O_4$ crystalline lattice, which in turn increased the lattice tension. This behavior is similar to Vegard's law for solid two-component metallic solutions, which predicts that the unit cell dimensions of the solid solution vary linearly with the solute component concentration [17, 18].

The initial cell and atomic position parameters used in the optimization process were taken from the Rietveld refinement results of $SrMo_{0.5}W_{0.5}O_4$ and $Sr_{(1-x)}Eu_xMo_{0.5}W_{0.5}O_4$. The scheelite structure is characterized by strontium atoms bonded to eight oxygen atoms, resulting in [SrO_8] clusters, and the molybdenum or tungsten atoms coordinated to four oxygen atoms in a tetrahedral configuration, i.e., forming [MoO_4] or [WO_4] cluster. The unit cells of each sample were modeled from the lattice parameter and atomic coordinate data obtained in the Rietveld refinement (Table 1) using the VESTA program [19], as shown in Figure S2 of supplementary information.

Table 1 Lattice parameters, crystallite size and quality coefficients of the Rietveld refinement for $SrMo_{0.5}W_{0.5}O_4$ and $Sr_{(1-x)}Eu_xMo_{0.5}W_{0.5}O_4$ samples

Sample	$SrMo_{0.5}W_{0.5}O_4$	$Sr_{0.99}Eu_{0.01}Mo_{0.75}W_{0.25}O_4$	$Sr_{0.98}Eu_{0.02}Mo_{0.75}W_{0.25}O_4$	$Sr_{0.96}Eu_{0.04}Mo_{0.75}W_{0.25}O_4$
System	Tetragonal	Tetragonal	Tetragonal	Tetragonal
Space group	I41/a	I41/a	I41/a	I41/a
a = b (Å)	5.410	5.411	5.408	5.406
c (Å)	11.99	11.97	11.97	11.97
c/a	2.22	2.21	2.21	2.21
V (Å^3)	351.100	350.500	350.100	349.700
D (nm)	22	18	16	17
ε ($\times 10^{-3}$)	1.09	1.31	1.53	1.43
X^2	1.905	1.489	1.539	1.577
R_p (%)	8.42	7.81	7.75	8.22
R_{bragg} (%)	6.80	6.95	5.48	7.38

Raman

The scheelite structure has $[XO_4]^{2-}$-type molecular ion units (X = Mo, W) with strong X-O covalent bonds and a weak coupling with the M^{2+} cation (M = Sr). The calculation of the group theory shows 26 different vibrations for the MXO_4 crystal with zero wave vector (k = 0), represented in Eq. (1) [20]:

$$\Gamma = 3A_g + 5A_u + 5B_g + 3B_u + 5E_g + 5E_u \quad (1)$$

The vibration for active Raman modes only is reduced to:

$$\Gamma = 3A_g + 5B_g + 5E_g \quad (2)$$

Modes *A* and *B* are not regenerated, and mode *E* is doubly degenerated. The subscripts "*g*" and "*u*" indicate parity under inversion in centimeter-symmetric crystals. A_g, B_g and E_g arise from the same movement as the MXO_4. Thus, the 13 Raman-active modes are expected, as presented by Eq. (2).

The Raman vibrational modes can be classified into two groups: external and internal modes. The first is known as the lattice phonon and it refers to the movement of M^{2+} cations in relation to the fixed units of the $[XO_4]^{2-}$ tetrahedrons. The second refers to the vibration inside the $[XO_4]^{2-}$ tetrahedral units, being considered the steady state of the center of mass. These tetrahedrons units have Td symmetry and consist of four internal modes ($v_1(A_1)$, $v_2(E_1)$, $v_3(F_2)$ and $v_4(F_2)$), a free rotation mode ($v_{f.r.}(F1)$) and a conversion mode (F_2) [21]. When the $[XO_4]^{2-}$ tetrahedrons have a scheelite structure, the point symmetry is reduced to S_4 [22–24].

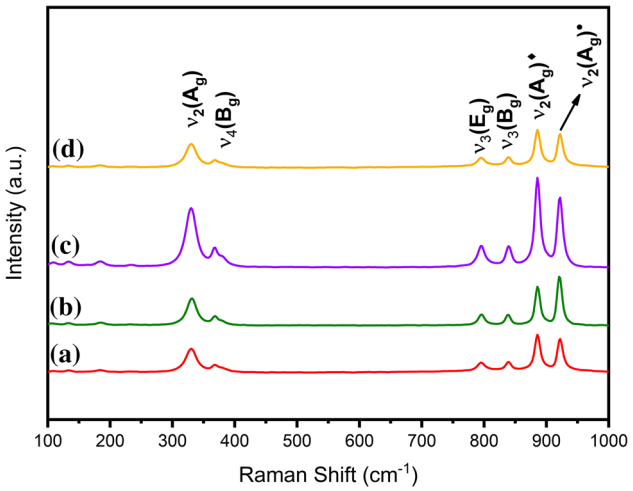

Figure 2 Raman spectra of: (a) $SrMo_{0.5}W_{0.5}O_4$, (b) $Sr_{0.99}Eu_{0.01}Mo_{0.5}W_{0.5}O_4$,, (c) $Sr_{0.98}Eu_{0.02}Mo_{0.5}W_{0.5}O_4$, and (d)$Sr_{0.96}Eu_{0.04}Mo_{0.5}W_{0.5}O_4$ particles.

Figure 2 shows the Raman spectra in the range between 100 and 1000 cm^{-1} for the $SrMo_{0.5}W_{0.5}O_4$ and $Sr_{(1-x)}Eu_xMo_{0.5}W_{0.5}O_4$ samples, respectively. There are eight vibrations recorded in Table 2. The $v_2(A_g)^\blacklozenge$ (at 884 cm^{-1}) and $v_2(A_g)^\bullet$ (at 918 cm^{-1}) modes are associated with $[MoO_4]^{2-}$ and $[WO_4]^{2-}$ vibration modes, respectively. A variation in the positioning of the vibration modes (cm^{-1}) caused by the formation of covalent bonds between Mo^{6+} (or W^{6+}) and O^{2-} ions in the $[MoO_4]^{2-}$ and $[WO_4]^{2-}$ tetrahedrons alter the efficient mass of the oscillating atoms [25].

Two high-frequency bands centered at 884 cm^{-1} for $SrMoO_4$ and 920 cm^{-1} for $SrWO_4$ are also present in $SrMo_{0.5}W_{0.5}O_4$ solid solutions, which correspond

Table 2 Raman active modes of $SrMo_{0.5}W_{0.5}O_4$ and $Sr_{(1-x)}Eu_xMo_{0.5}W_{0.5}O_4$

Sample Lattice mode symmetry C_{4h}^6	E_g (cm^{-1})	E_g (cm^{-1})	B_g (cm^{-1})	A_g (cm^{-1})	B_g (cm^{-1})	E_g (cm^{-1})	B_g (cm^{-1})	$A_g^{\blacklozenge}$/ $A_g^{\bullet}$ (cm^{-1})
$SrMo_{0.5}W_{0.5}O_4$	133	185	234	330	367	795	839	885/ 924
$Sr_{0.99}Eu_{0.01}Mo_{0.75}W_{0.25}O_4$	134	184	–	330	369	795	838	884/ 921
$Sr_{0.98}Eu_{0.02}Mo_{0.75}W_{0.25}O_4$	132	184	234	328	369	793	841	884/ 925
$Sr_{0.96}Eu_{0.04}Mo_{0.75}W_{0.25}O_4$	134	184	–	328	369	795	841	886/ 921

to intense peaks in the Raman (Ag) mode and are assigned to the symmetric stretching $v_2(A_g)$ of the bonds [← O ← M → O →] (M = Mo and W), while the two Raman (Bg and Eg internal) modes at 841 and 792 cm^{-1} are attributed to the asymmetric stretching v_3(F2) of the bonds (→ O → M → O →).

FEG-SEM

Figure 3 shows the FEG-SEM images of the $SrMo_{0.5}W_{0.5}O_4$ samples obtained by MHM. Figure 3 displays different morphology types for the $SrMoO_4$ sample, where it is possible to identify distinct shapes: microrice, microflowers and microspheres. The formation of microflowers occurs by joining the petals from the central region, where a radial growth can be observed. New petals are added with the morphology development, assuming the shape of microflowers. The growth of these petals occurs in an Ostwald ripening process [26]. The high-resolution FEG-SEM image shows microspheres with rough surfaces composed by numerous irregular nanocrystals. The presence of particles with irregular spherical appearance formed by several smaller particles is observed.

According to the morphologies presented in Fig. 3 obtained by MHM with the Mo:W variation, it can be inferred that the $SrMo_{0.5}W_{0.5}O_4$ microstructures were obtained from a growth mechanism consisting of two stages: (i) nucleation which constitutes the initial stage; and (ii) posterior crystal growth [27]. The initial reaction stage is formed by small crystalline nuclei in

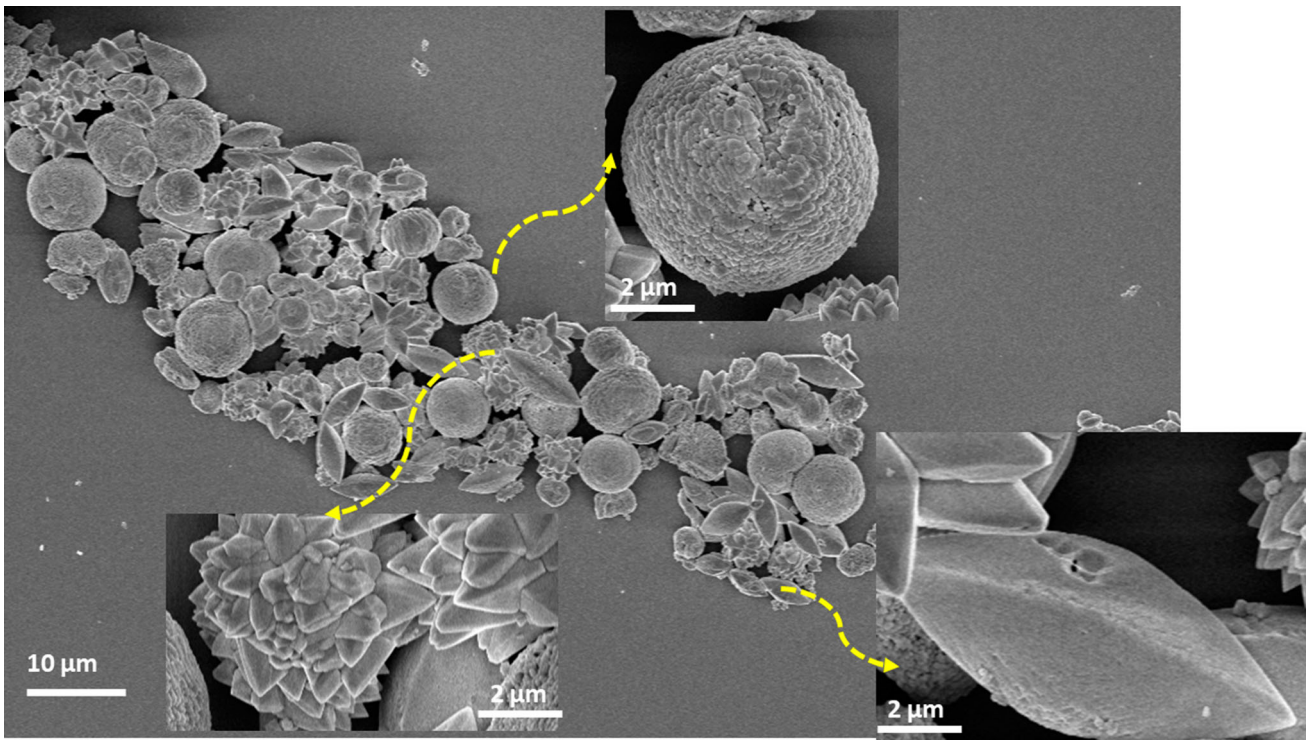

Figure 3 FEG-SEM images of $SrMo_{0.5}W_{0.5}O_4$ particles.

the supersaturated solution, which function as crystallization centers. However, a strong Coulombic electrostatic attraction occurs between Sr^{2+} and WO_4^{2-}/MoO_4^{2-} ions due to differences in the electronic density between them, resulting in forming the first WO_4/MoO_4 precipitates or nucleation seeds. Numerous nanocrystals are formed from the anisotropic growth of the crystalline nuclei. These nanocrystals become larger at the expense of smaller crystals through the Ostwald ripening process [26]. According to Xia et al. [27], the smaller crystals continue to grow by layer stacking in order to minimize the energy in the solution. The final microstructures of the growth process are completed through aggregation and targeted fixation of the nanoparticles. The self-assembly of nanoparticles is of great importance for the final morphology of $SrMo_{0.5}W_{0.5}O_4$ particles.

Several research groups have studied the development of different morphologies based on combining nanoparticle construction units [28–30]. However, the formation mechanism of these crystals is not yet well defined, with the Ostwald ripening process being the most referenced approach. This phenomenon happens when large crystallites grow at the expense of small ones through the diffusion of ions, atoms or molecules, indicating that it is responsible for the main path of crystal growth. Although the crystal growth process is complex, some studies have focused on the growth and self-assembly of nanoparticles. Nevertheless, some factors which affect the growth process of crystals, such as the attraction of the crystal phase, the electrostatic and dipolar field interactions in the crystal aggregates, the Van de Waals forces and the hydrophobic interactions, remain unclear [31]. It is worth mentioning that the self-assembly and Ostwald ripening processes are responsible for forming the morphologies presented by $SrMo_{0.5}W_{0.5}O_4$.

Analyses of UV–Vis absorption spectroscopy and optical band gap values

Figure S3 of supplementary information represents the diffuse reflectance spectra of the $SrMo_{0.5}W_{0.5}O_4$ and $Sr_{(1-x)}Eu_xMo_{0.5}W_{0.5}O_4$ samples obtained between 200 and 800 nm. According to the results, the samples showed an absorption range at short wavelengths (200–300 nm) attributed to the absorption of the host matrix, with the exception of the $SrMo_{0.5}W_{0.5}O_4$ sample, which exhibited a shift in the curve to a high-energy region and presented a much smaller absorption band (200–270 nm). It appears that the adjustment between the Mo:W amounts promoted widening of the sample absorption bands, leading to displace the curves to greater wavelength values.

According to Spassky et al. [32], the band around 280 nm is attributed to the electronic transitions inside the $(MoO_4)^{2-}/(WO_4)^{2-}$ tetrahedrons. The reflectance gradually increases between 300 and 360 nm, reaching 93% around 380 nm. The absorption intensity around 280 nm (4.42 eV) represents approximately 85%, thus indicating that the material excitation may be more efficient in this region. In addition, the band gap energy of $SrMoO_4$ and $SrWO_4$ is around 3.90 and 4.80 eV, respectively [9]. From Figure S3, it can be seen that the introduction of Eu^{3+} into the $Sr_{(1-x)}Eu_xMo_{0.5}W_{0.5}O_4$ matrix promotes an increase in the absorption band amplitude with a curved shift to the right close to 342 nm. The bands identified by * are attributed to the Eu^{3+} (*f-f*) transitions $^7F_0 \rightarrow {}^5L_6$, $^7F_0 \rightarrow {}^5D_2$ and $^7F_1 \rightarrow {}^5D_1$, located at 393, 462 and 535 nm, respectively [8], proving the existence of Eu^{3+} in the $SrMo_{0.5}W_{0.5}O_4$ structure.

The band gap energy values (E_{gap}) were calculated using the Kubelka–Munk Equation [33], which is based on the transformation of diffuse reflectance measurements to precisely estimate E_{gap} values [34]. The Kubelka–Munk Eq. (3) for any wavelength is described by:

$$\frac{K}{S} = \frac{(1-R)^2}{2R} = F(R), \tag{3}$$

in which *F(R)* is the Kubelka–Munk function or absolute reflectance of the sample in this work, barium sulfate ($BaSO_4$) was adopted as a standard sample for reflectance measurements (R = Rsample/R($BaSO_4$)), *R* is the reflectance, *K* is the molar absorption coefficient and *S* is the dispersion coefficient. The band gap and the absorption coefficient of semiconductor oxides can be calculated by Eq. (4) [35]:

$$\alpha hv = C_1\left(hv - E_{gap}\right)^n, \tag{4}$$

in which α is the linear absorption coefficient of the material, *hv* is the photon energy, C_1 is a proportionality constant, E_{gap} is the band gap and *n* is a constant associated with different types of electronic transitions ($n = 1/2$ for direct allowed, $n = 2$ for indirect allowed, $n = 1.5$ for direct prohibited and

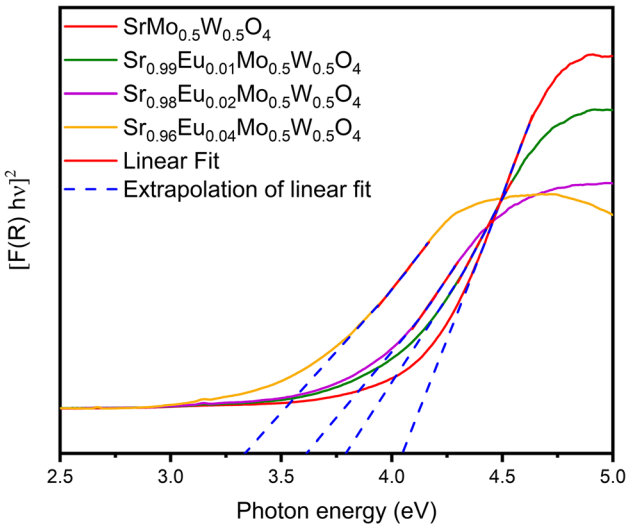

Figure 4 Band gap energy of $SrMo_{0.5}W_{0.5}O_4$ and $Sr_{(1-x)}Eu_xMo_{0.5}W_{0.5}O_4$ samples.

n = 3 for indirect prohibited). According to theoretical calculations reported in the literature [36], scheelite-type crystals (ABO_4) exhibit an absorption spectrum governed by direct electronic transitions. Figure 4 shows the band gap energy values of the $SrMo_{0.5}W_{0.5}O_4$ and $Sr_{(1-x)}Eu_xMo_{0.5}W_{0.5}O_4$ samples. These values were calculated according to the Tauc relationship and are shown in Table 3.

There is a downward trend in the E_{gap} for samples doped with Eu^{3+}. This behavior can be justified by the replacement of Eu^{3+} by Sr^{2+} in the $SrMo_{0.5}W_{0.5}O_4$ matrix. In order to maintain the electronic neutrality of the material, the appearance of defects such as oxygen vacancy (V_O) is possible since cations have different valences. The presence of (V_O) causes the appearance of intermediate levels in the band gap, resulting in a decrease in the E_{gap} value. According to Pereira et al. [37], different types of structural defects are associated with $SrWO_4$:Eu^{3+} crystals. These defects can also be attributed to oxygen vacancies by the introduction of Eu^{3+} ions. These authors reported that the band gap behavior can be justified by the formation of strontium vacancies (V''_{Sr}) and an oxygen-vacancy complex capable of causing three changes in different ways: V_O^x (neutral), V_O (singly ionized) and V_O (doubly ionized). V_O^x are able to donate up to two electrons, V_O are donors or capture only one electron, and V_O are not able to donate electrons, but can receive up to two electrons. These oxygen vacancies act as defects in the crystal structure and can be stabilized by compensating the load on the lattice. The need for load compensation and the influence of synthesis conditions (temperature and treatment times) cause lattice distortion. Gonçalves et al. [38] observed a downward trend in the E_{gap} values with the replacement of Ca^{2+} by Eu^{3+} ions in $CaWO_4$ associated with an increase in intermediate energy levels between the valence and conduction bands. They also studied the presence of new electronic levels resulting from the addition of 4f orbitals of Eu^{3+} ions into the crystalline lattice. Other factors that may influence E_{gap} values are related to the morphology, shape and size of the particles.

Photoluminescence

Figure 5a shows the emission spectra of PL of the $SrMo_{0.5}W_{0.5}O_4$ sample at room temperature, excited at a wavelength (λ_{exc}) of 325 nm. It appears that the sample has a broadband profile in all spectra. It is known that the positioning and intensity of PL emission vary with some factors, such as particle morphology, size and surface defects [39]. According to Wang et al. [40], the particle morphology and size interfere with the excited transporters from the valence to the conduction band, subsequently leading to luminescence variations. Li et al. [41] associate this

Table 3 Gap energy, photometric parameters and % of the components of the deconvolution of the PL

	$SrMo_{0.5}W_{0.5}O_4$	$Sr_{0.99}Eu_{0.01}Mo_{0.75}W_{0.25}O_4$	$Sr_{0.98}Eu_{0.02}Mo_{0.75}W_{0.25}O_4$	$Sr_{0.96}Eu_{0.04}Mo_{0.75}W_{0.25}O_4$
E_{gap} (eV)	4.15	4.05	3.77	3.61
CIE (x,y)	(0.32, 0.39)	(0.57, 0.37)	(0.61, 0.36)	(0.63, 0.35)
CCT (K)	6060	1469	1227	1087
CRI (%)	80	78	80	78
Purity (%)	12	84	92	97
Color	Branco	Vermelho	Vermelho	Vermelho
LER	311	273	265	252

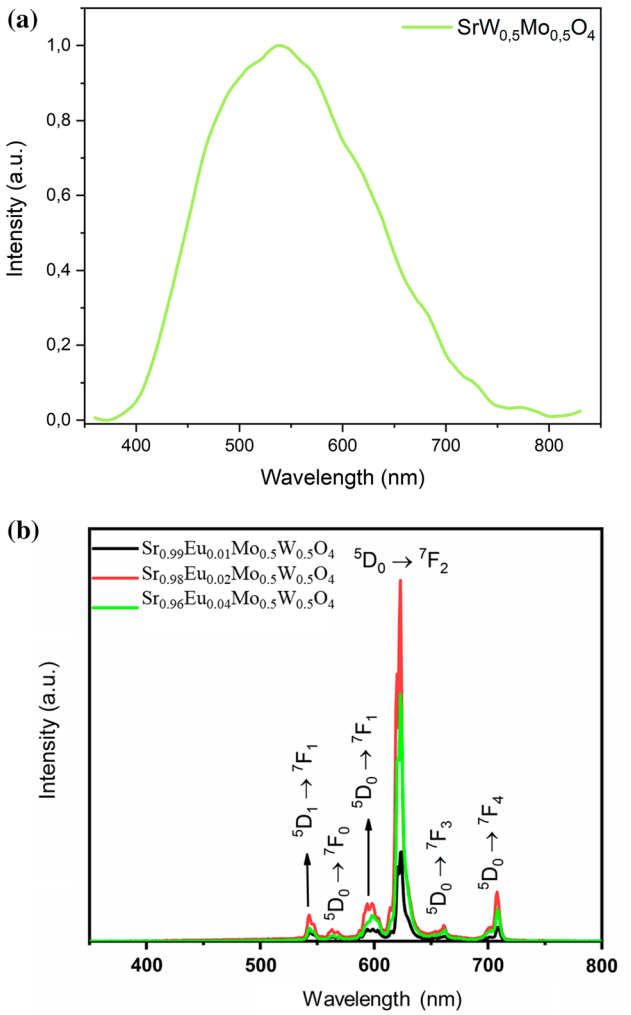

Figure 5 Emission spectra of (a) $SrMo_{0.5}W_{0.5}O_4$, (b) $Sr_{(1-x)}Eu_xMo_{0.5}W_{0.5}O_4$ samples, λ_{exc} = 325 nm.

broadband with the intrinsic luminescent behavior of the $[MoO_4]^{2-}$ group with green emission resulting from the transition $^3T_1$, $^3T_2 \rightarrow {}^1A_1$ [42]. The replacement of $Mo^{6+} \rightarrow W^{6+}$ improves the electron transfer process within the clusters $[WO_4]^{2-}$ due to the strong hybridization of the W (5d) and O (2p) orbitals. The wide visible emission originates from the charge-transfer transition between the O(2p) orbital and the empty d orbital of the $[MO_4]^{2-}$ (M = Mo and W) tetrahedral structure, with excitation energies located within the band gap [43]. The one ground state is $^1A_1$, and the four single excited states are $^1A(^1T_1)$, $^1E(^1T_1)$, $^1E(^1T_2)$, and $^1B(^1T_2)$ [44]. This behavior can be associated with specific structural arrangements of the $[WO_4]$ or $[MoO_4]$ clusters. Oliveira et al. [45] discussed the stability of different surfaces of the solid solution BaW_{1-x} Mo_xO_4 as a function of the local coordination of the Mo^{6+} and W^{6+} ions. The exposure of specific crystal planes is associated with how these cations are sub-coordinated. With these structural changes, it is possible to modulate the electronic structure and the surface energy values, to evaluate the order of stability of the crystal planes.

The PL emission of scheelite-type molybdates and tungstates is not fully understood. There are several strands that try to explain the photoluminescent behavior of these groups of materials. PL properties can be caused by several possible mechanisms, and the spectra can be associated with different components. Considering the spectra characteristics, such as band position and PL intensity, it can be inferred that the position of the band refers to an intrinsic property in molybdates and tungstates, sensitive to electronic charge transfer between different energy states within the $[MoO_4]^{2-}$ /$[WO_4]^{2-}$ clusters, and the structural arrangement. These load transitions, energy states and structural arrangements are influenced by distortions in the $[MoO_4]^{2-}$/$[WO_4]^{2-}$ clusters. The PL intensity strongly depends on the morphology, distribution, degree of aggregation and orientation of the particles, as well as the surface defects and different excitation wavelengths [46]. Some electrons located in the 2p (O) states are promoted to the 4d (Mo) or 5d (W) state by the absorption of photons ($h\nu$) during the excitation process, forming excitons (electron trapping by holes). The photon emission process occurs when an electron located in the 4d molybdenum state decays to the 2p state of oxygen.

Figure 5b shows the PL spectra of the $Sr_{(1-x)}Eu_{x-}Mo_{0.5}W_{0.5}O_4$ samples (x = 1, 2 e 4 mol%). It can be noticed that only Eu^{3+} transitions are evident and that there was no interference from the matrix. In addition, it appears that the energy transfer between 4d (or 5d) (Mo / W) → 4f (Eu^{3+}) occurred perfectly. The *f-f* transitions of Eu^{3+} are $^1D_1 \rightarrow {}^7F_1$ and $^1D_0 \rightarrow {}^7F_J$ (J = 0, 1, 2 and 3), located at 543, 562, 597, 623, 662 and 706 nm, respectively. The dominant red emission ($^1D_0 \rightarrow {}^7F_2$) centered at 623 nm is attributed to the electric dipole, while the other weak emission ($^1D_0 \rightarrow {}^7F_1$) located at 597 nm is attributed to the magnetic dipole transition. The energy levels of Eu^{3+} are protected by the shielding effect of the $5s^25p^6$ orbitals, with no change in the position of the Eu^{3+} bands caused by the crystal field. The transition $^1D_0 \rightarrow {}^7F_2$ is allowed when Eu^{3+} ions are positioned in crystallographic sites without inversion symmetry

[47]. When the Eu^{3+} ions occupy the non-inversion center sites, the transition $^1D_0 \rightarrow {}^7F_2$ tends to be relatively stronger, in contrast to the very weak transition $^1D_0 \rightarrow {}^7F_1$. The site symmetry around Eu^{3+} in the $SrMo_{0.5}W_{0.5}O_4$ matrix can be estimated through the asymmetry ratio (R) in order to assess the distortion degree of the inversion symmetry of the local crystalline environment. The asymmetry ratio is calculated from the relationship between the integrated intensities of the transitions $^1D_0 \rightarrow {}^7F_2$ (I_2) and $^1D_0 \rightarrow {}^7F_1$ (I_1). The calculated *R* values for $Sr_{0.99}Eu_{0.01}Mo_{0.5}W_{0.5}O_4$, $Sr_{0.98}Eu_{0.02}Mo_{0.5}W_{0.5}O_4$ and $Sr_{0.96}Eu_{0.04}Mo_{0.5}W_{0.5}O_4$ were 3.98, 4.82 and 5.28, respectively. It can be seen that an increase in the *R* value occurs with the increase in the Eu^{3+} concentration in $SrMo_{0.5}W_{0.5}O_4$. Eu^{3+} ions prefer to enter asymmetric centers of A^+ cations. The introduction of Eu^{3+} produces a noticeable inversion symmetry breakdown in the ligand coordination environment of the Eu^{3+} lattice site, resulting in a variation of the asymmetry ratio. Lower *R* values usually indicate higher symmetry values of the crystal field.

Gonçalves et al. [38] related the PL intensity and the amount of Eu^{3+} ions in the matrix to the coordination environment and/or changes in the shape and size of the crystals. Sharma and Singh [5] showed that the dipole–dipole interaction increases as a function of Eu^{3+} concentration, which consequently increases the cross-relaxation between Eu^{3+} ions when the average distance between them is less than a critical value. This critical value depends on the crystalline structure and particle size of the host matrix.

The $Sr_{0.98}Eu_{0.02}Mo_{0.5}W_{0.5}O_4$ sample reveals a higher intensity of photoluminescence. A significant drop in intensity is perceived for a higher Eu^{3+} concentration (%). This behavior is known as quenching and is motivated by the approximation of Eu^{3+} to the structure, thus favoring non-radioactive emission as opposed to photon emission. We used the Blasse Eq. (5) to calculate the critical distance (CD) between Eu^{3+} ions [48]:

$$CD \cong 2\left(\frac{3V}{4Xc\pi Z}\right)^{\frac{1}{3}}, \quad (5)$$

in which *V* is the volume of the unit cell, *Xc* is the critical Eu^{3+} concentration and *Z* is the number of atoms per unit cell. The terms for $Sr_{0.98}Eu_{0.02}Mo_{0.5}W_{0.5}O_4$ assume the following values: V = 349.94 $Å^3$, Xc = 0.02 mol and Z = 4, and the estimated value CD = 20.29 Å. As CD is greater than 5 Å, it means

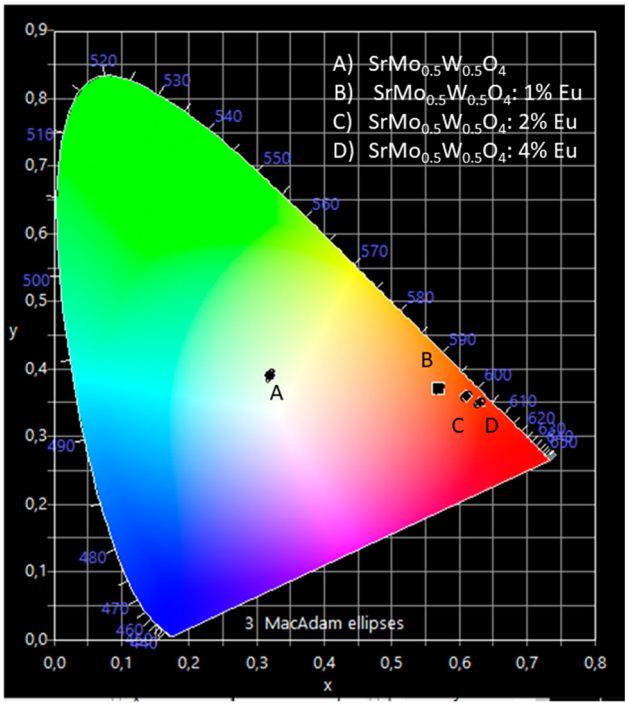

Figure 6 Chromaticity diagram of $SrMo_{0.5}W_{0.5}O_4$ and $Sr_{(1-x)}Eu_xMo_{0.5}W_{0.5}O_4$ samples.

that the energy transfer process occurs through multipolar interactions [49]. These types of interactions are responsible for suppressing photoluminescence and can be classified as dipole–dipole or quadrupole–quadrupole interactions.

Figure 6 depicts the chromaticity diagram, indicating the chromaticity coordinates with the digital photographs of the presented emissions of $SrMo_{0.5}W_{0.5}O_4$ and $Sr_{(1-x)}Eu_xMo_{0.5}W_{0.5}O_4$. The $SrM_{0.5}W_{0.5}O_4$ samples show emission in the white region due to the adjustable contribution of simultaneous emissions in the blue, green and red regions. There is a strong emission in the red region for samples doped with Eu^{3+} due to the transition $^5D_0 \rightarrow {}^7F_2$ at 623 nm. The increase in the % of Eu^{3+} favors the increase in purity. As shown in Fig. 6, the sample with 4% of Eu^{3+} is located very close to the end of the red region with maximum purity. The calculated values of color purity for the $Sr_{(1-x)}Eu_xMo_{0.5}W_{0.5}O_4$ samples reach the order of 97%.

The results of the color reproduction index (CRI) obtained were in the range of 78 to 80%. The values indicate that the emissions ensure excellent reliability in the color integrity of the objects when illuminated by the samples produced. The luminous efficiency of radiation (LER) of the samples was also investigated.

The results revealed high LER values (322 $lm.W^{-1}$), a characteristic desired for use in WLEDs. Molybdates and tungstates activated with Eu^{3+} ions present a high luminous efficiency around 250–315 lm/W^{-1} [50–52] due to the narrow emission ($^5D_0 \rightarrow {}^7F_J$). However, the number of red-emitting phosphors suitable for high LER applications is still small. Within this group of materials, Eu^{3+} is the most used activator ion [53] because it has emissions between 610 and 660 nm. Light conversion using a phosphor with emission characteristics of narrow lines with wavelengths aligned with the sensitive area of the human eye may be more efficient for increasing LER.

The ratio of the emitted luminous flux in lumen and the power used in watts describes the LER. The LER is a measure expressed in lumens per visible watts used to estimate how brightly the radiation is perceived to be by the average human eye. The LER is determined by the spectral distribution S (λ) of the source, as given by Eq. (6):

$$LER = \frac{Km \int_{360}^{830} V(\lambda)S(\lambda)d(\lambda)}{\int_{360}^{830} S(\lambda)d(\lambda)}[lm.W^{-1}], \quad (6)$$

in which $V(\lambda)$ = eye sensitivity curve and Km = 683 [l lm W^{-1}]], which is the highest possible efficiency that can ever be obtained from a light source [54]. Table 3 presents all the photometric parameters of the $SrMo_{0.5}W_{0.5}O_4$ and $Sr_{(1-x)}Eu_xMo_{0.5}W_{0.5}O_4$ samples. The high LER and CRI values indicate that the synthesized material has fundamental properties for applicability in WLEDs. The LER decreases as the Eu^{3+} concentration increases, meaning when the emission band changes to red. This is caused by a smaller overlapping of the emission spectra with the human eye sensitivity curve [55]. Strong UV absorption is required to improve the CRI and LER photometric parameters for producing white light. Molybdates activated with rare earth ions are gaining more and more attention in the research field due to their strong emission of visible light under excitation in UV [56]. Furthermore, phosphor molybdates activated with rare earth ions have excellent chemical stability and high luminous efficiency, characteristics necessary for developing solid-state lighting devices.

Conclusion

The $SrMo_{0.5}W_{0.5}O_4$ and $Sr_{(1-x)}Eu_xMo_{0.5}W_{0.5}O_4$ phosphors were synthesized by MHM. XRD patterns revealed that all samples have pure tetragonal phase. The doping process in the replacement of Mo^{6+} ions (W^{6+}) by Eu^{3+} ions was successful, not showing the appearance of secondary phases. The different morphological aspects of $SrMo_{0.5}W_{0.5}$ O_4 particles were evaluated and a mechanism for crystal formation was proposed from the nucleation and subsequent growth stages of the particles. The morphologies presented are the result of cooperative self-assembly processes and the self-assembly and Ostwald ripening cooperative processes. The particles presented different morphologies according to the chemical composition of the samples. $Sr_{(1-x)}Eu_xMo_{0.5}W_{0.5}O_4$ showed intense luminescence in the red region due to the predominant transition $^5D_0 \rightarrow {}^7F_2$ at 623 nm. According to the calculated asymmetry ratio, increasing Eu^{3+} concentration causes a decrease in symmetry in the ligand coordination environment of the Eu^{3+} lattice site. The effect of quenching concentration was investigated and concentrations greater than 2 mol % cause suppression of photoluminescence due to the energy transfer process occurs through multipolar interactions. The samples demonstrated a high degree of purity, reaching the order of 97%. The emission in the white region was observed in the $SrMo_{0.5}W_{0.5}O_4$ sample, which showed simultaneous emissions in the blue, green and red regions with a spectrum with a broadband profile. The photometric quality parameters (CIE, CRI and LER) obtained according to the spectral energy functions indicate that the $SrMo_{0.5}W_{0.5}O_4$ and $Sr_{(1-x)}Eu_xMo_{0.5}W_{0.5}O_4$ samples can be applied in solid-state lighting devices.

Acknowledgements

The authors wish to thank the financial support of the following Brazilian research funding agencies: the National Council for Scientific and Technological Development (*CNPq*), the Coordination for the Improvement of Higher Education Personnel (*CAPES*) and the Graduate Program in Materials Science and Engineering (*PPGCEM/UFRN*).

Declarations

Conflict of interest The authors declare that they have no conflict of interest.

Supplementary Information: The online version contains supplementary material available at https://doi.org/10.1007/s10853-022-07203-x.

References

[1] Bünzli JCG, Comby S, Chauvin AS, Vandevyver CD (2007) New opportunities for lanthanide luminescence. J Rare Earths 25(3):257–274

[2] Li P, Yang Z, Wang Z, Guo Q, Li X (2008) Luminescent characteristics of $Ba_3Y_2(BO_3)_4:Eu^{3+}$ phosphor for white LED. J Rare Earths 26:44–47

[3] Singh NS, Ningthoujam RS, Devi LR, Yaiphaba N, Sudarsan V, Singh SD, Vatsa RK, Tewari R (2008) Luminescence study of Eu^{3+} doped $GdVO_4$ nanoparticles: concentration, particle size, and core/shell effects. J Appl Phys 104:104307–104309

[4] Li LZ, Yan B, Lin LX, Zhao Y (2011) Solid state synthesis, microstructure and photoluminescence of Eu^{3+} and Tb^{3+} activated strontium tungstate. J Mater Sci Mater Electron. 22:1040–1045

[5] Gayatri Sharma K, Singh NR (2012) Synthesis of $CaWO_4:Eu^{3+}$ phosphor powders via ethylene glycol route and its optical properties. J Rare Earths 30:310–314

[6] Zhang Y, Wang B, Liu Y, Bai G, Fub Z, Liu H (2021) Upconversion luminescence and temperature sensing characteristics of $Yb^{3+}/Tm^{3+}:KLa(MoO_4)_2$ phosphors. Dalton Trans 50:1239

[7] Liu H, Zuo C, Liu Y, Gao G, Liu D, Wang T, Liu T, Zhang Y (2019) Optical thermometry through infrared excited green upconversion of $KLa(MoO_4)_2:Yb^{3+}$ /Er^{3+} phosphor. J Lumin 207:93

[8] Janulevicius M et al (2016) Luminescence and luminescence quenching of highly efficient Y2Mo4O15:Eu3+ phosphors and ceramics. Sci Rep 6(1):26098

[9] GuangJia JL, Qin X, Zhang M, Chen L, Sun Y, Gao L, Zhang C (2016) Uniform $SrMoO_4:Ln^{3+}$ (Ln = Eu, Tb, Dy, and Sm) hierarchical microspheres: Facile synthesis and luminescence properties. Mater Lett 165:160–164

[10] Huang F et al (2015) Yb3+/Er3+ co-doped CaMoO4: a promising green upconversion phosphor for optical temperature sensing. J Alloy Compd 639:325–329

[11] Parchur AK, Ningthoujam RS, Rai SB, Okram GS, Singh RA, MohitTyagi SC, Gadkari RT, Vatsa RK (2011) Luminescence properties of Eu^{3+} doped $CaMoO_4$ nanoparticles. Dalton Trans 40:7595

[12] Suneeta P, Rajesh Ch, Ramana MV (2018) Synthesis and characterization of rare-earth–doped calcium tungstate nanocrystals. Eur Phys J Plus 133:59

[13] Pinatti IM, Nogueira IC, Pereira WS, Pereira PFS, Gonçalves RF, Varela JA, Longoc E, Rosa ILV (2015) Structural and photoluminescence properties of Eu^{3+} doped α-Ag_2WO_4 synthesized by the green coprecipitation methodology. Dalton Trans 44:17673

[14] Gai S et al (2014) Recent progress in rare earth micro/nanocrystals: soft chemical synthesis, luminescent properties, and biomedical applications. Chem Rev 114(4):2343–2389

[15] JustynaCzajka ZP, Szczeszak A, Lis S (2018) Structural, morphology and luminescence properties of mixed calcium molybdate-tungstate microcrystals doped with Eu^{3+} ions and changes of the color emission chromaticity. Opt Mater 84:422–426

[16] Toby BH (2001) EXPGUI, a graphical user interface for GSAS. J Appl Crystallogr 34:210–213

[17] McKelvy MJ et al (2001) Magnesium hydroxide dehydroxylation: in situ nanoscale observations of lamellar nucleation and growth. Chem Mater 13(3):921–926

[18] Motta FV et al (2013) Preparation and photoluminescence characteristics of In(OH)3:xTb3+ obtained by microwave-assisted hydrothermal method. J Alloys Compd 553(Supplement C):338–342

[19] Momma K, Izumi F (2011) VESTA 3 for three-dimensional visualization of crystal, volumetric and morphology data. J Appl Crystallogr 44:1272–1276

[20] TitipunThongtem SK, Kuntalue B, Phuruangrat A, Thongtem S (2010) Luminescence and absorbance of highly crystalline $CaMoO_4$, $SrMoO_4$, $CaWO_4$ and $SrWO_4$ nanoparticles synthesized by co-precipitation method at room temperature. J Alloys Compd 506:475–481

[21] Voron'ko YK, Sobol AA (2005) Influence of cations on the vibrational spectra and structure of $[WO_4]$ complexes in molten tungstates. Inorg Mater 41:420–428

[22] Pereira PFS, de Moura AP, Nogueira IC, Lima MVS, Longo E, de Sousa Filho PC, Serra OA, Nassar EJ, Rosa ILV (2012) Study of the annealing temperature effect on the structural and luminescent properties of $SrWO_4$: Eu phosphors prepared by a non-hydrolytic sol–gel process. J Alloys Compd 526:11–21

[23] Sujatha RA et al (2019) Structural and non-linear optical response of Er3+ doped SrMoO4 nanostructures. Appl Surf Sci 490:260–265

[24] Adhikari R et al (2014) Understanding the infrared to visible upconversion luminescence properties of Er3+/Yb3+ co-doped BaMoO4 nanocrystals. J Solid State Chem 216:36–41
[25] Basiev TT, Sobol AA, Voronko YK, Zverev PG (2000) Spontaneous Raman spectroscopy of tungstate and molybdate cryystals for Ramn lasers. Opt Mater 15:205–216
[26] Tao Wu, Liu Y, Yinong Lu, Wei Ling, Gaoa Hong, Chen Hu (2013) Morphology-controlled synthesis, characterization, and luminescence properties of $KEu(MoO_4)_2$ microcrystals. CrystEngComm 15:2761–2768
[27] Wenpeng Xia YZ, Shanshan Hu, Xiong Jie, Tang J, Yan Jun (2018) Self-assembled hierarchical architecture of tetragonal $AgLa(MoO_4)_2$ crystals: hydrothermal synthesis, morphology evolution and luminescence properties. CrystEngComm 20:1832–1843
[28] Ghosh SK, Rout SK, Tiwari A, Yadav P, Sczancoski JC, Filho MGR, Cavalcante LS (2015) Structural refinement, Raman spectroscopy, optical and electrical properties of $(Ba_{1-x}Sr_x)MoO4$ ceramics. J Mater Sci: Mater Electron 26:8319–8335
[29] Cao Y, Hu P, Ji D (2013) Phase- and shape-controlled hydrothermal synthesis of CdS nanoparticles, and oriented attachment growth of its hierarchical architectures. Appl Surf Sci 265:771–777
[30] Zhou Y, He X-H, Yan B (2014) Self-assembled RE2(MO4)3:Ln3+ (RE = Y, La, Gd, Lu; M = W, Mo; Ln = Yb/Er, Yb/Tm) hierarchical microcrystals: Hydrothermal synthesis and up-conversion luminescence. Opt Mater 36:602–607
[31] Lv W, He W, Wang X, Niu Y, Cao H, Dickerson JH, Wang Z (2014) Understanding the oriented-attachment growth of nanocrystals from an energy point of view: a review. Nanoscale 6:2531–2547
[32] Spassky DA, Vasil'Ev AN, Kamenskikh IA, Mikhailin VV, Savon AE, Hizhnyi YuA, Nedilko SG, Lykov PA (2011) Electronic structure and luminescence mechanisms in $ZnMoO_4$ crystals. J Phys Condens Matter Inst Phys. 23:365501
[33] Kubelka P, Munk F (1931) Ein Beitrag Zur Optik Der Farbanstriche. Zeitschrift für Technische Physik 12:593–601
[34] Morales AE, Mora ES, Pal U (2007) Use of diffuse reflectance spectroscopy for optical characterization of un-supported nanostructures. Revista Mexicana de Física 56:18–22
[35] R.S.R., *Semiconductors*. Vol. 2nd edition 1978, London.
[36] Zhang Y, Holzwarth NAW, Williams RT (1998) Electronic band structures of the scheelite materials CaMoO4, CaWO4, PbMoO4, and PbWO4. Phys Rev B 57:12738–12750
[37] Pereira PFS, Nogueria IC, Longo E, Nassar EJ, Rosa ILV, Cavalcante LS (2015) Rietveld refinement and optical properties of $SrWO_4:Eu^{3+}$ powders prepared by the non-hydrolytic sol-gel method. J Rare Earths 33:113–126
[38] Gonçalves RF, Cavalcante LS, Nogueira IC, Longo E, Godinho MJ, de Sczancoski JC, Mastelaro VR, Pinatti IM, Rosa ILV, Marques APA (2015) Rietveld refinement, cluster modelling, growth mechanism and photoluminescence properties of $CaWO_4:Eu^{3+}$ microcrystals. CrystEngComm 17:1654–1666
[39] Li B, Zhang H, Lan A, Tang HT (2015) One-dimensional $CdWO_4.Tb^{3+}$ nanofibers: electrospinning fabrication and luminescence. Chem Phys Lett 636:22
[40] Wang WS, Zhen L, Xu CY, Shao WZ (2009) Room temperature synthesis, growth mechanism, photocatalytic and photoluminescence properties of cadmium molybdate core–shell microspheres. Cryst Growth Des 9:1558
[41] Li D, Huang Z, Nie Z, Zhang L, Bai Y, Zhang X, Song Y, Wang Y (2015) Anomalous upconversion luminescence of $SrMoO_4:Yb^{3+}/Er^{3+}$ nanocrystals by high excited state energy transfer. J Alloys Compd 650:799–804
[42] Lianping Chen YG (2007) Mechanisms and applications of cell electrochemical technique to prepare luminescent $SrMoO_4$ thin films. Chem Eng J 131:181–185
[43] Phuruangrat A, Thongtem T, Thongtem S (2012) Precipitate synthesis of $BaMoO_4$ and $BaWO_4$ nanoparticles at room temperature and their photoluminescence properties. Superlatt Microstruct 52:7–83
[44] Gao ZY, Wei SUN, Hu YH, Liu XW (2013) Surface energies and appearances of commonly exposed surfaces of scheelite crystal. T Nonferr Metal Soc 23:2147–2152
[45] Oliveira MC, Juan A, Gracia L, De Oliveira MS, Mercury JMR, Longo E, Nogueira IC (2019) Geometry, electronic structure, morphology, and photoluminescence emissions of $BaW_{1-x}Mo_xO_4$ (x=0, 0.25, 0.50, 0.75, and 1) solid solutions: Theory and experiment in concert. Appl Surf Sci 463:907–917
[46] Marques VS, Cavalcante LS, Sczancoski JC, Alcântara AFP, Orlandi MO, Moraes E, Longo E, Varela JA, Siu Li M, Santos MRMC (2010) Effect of different solvent ratios(water/ethylene glycol) on the growth process of $caMoO_4$ crystals and their optical properties. Crystal Growth Desig 10:4752
[47] Chen Y, Yang HK, Park SW, Moon BK, Choi BC, Jeong JH, Kim KH (2012) Characterization and photoluminescent enhancement of Li+ corporation effect on $CaWO_4:Eu^{3+}$ phosphor. J Alloys Compd 511:123–128
[48] Blassse G (1986) Energy transfer between inequivalent Eu^{2+} ions. J Solid State Chem 62:207–211
[49] Kang F, Zhang Y, Peng M (2015) Controlling the energy transfer via multi luminescent centers to achieve white light/tunable emissions in a single-phased X2-type Y2SiO5:

Eu3+, Bi3+ phosphor for ultraviolet converted LEDs. Inorg Chem 54:1462–1473

[50] Grigorjevaite J, Katelnikovas A (2016) Luminescence and luminescence quenching of $K_2Bi(PO_4)(MoO_4):Eu^{3+}$ phosphors with efficiencies close to unity. ACS Appl Mater Int 8:31772–31782

[51] Grigorjevaite J, Ezerskyte E, Minderyte A, Stanionyte S, Juskenas R, Sakirzanovas S, Katelnikovas A (2019) Optical properties of red-emitting $Rb_2Bi(PO_4)(MoO_4):Eu^{3+}$ powders and ceramics with high quantum efficiency for white LEDs. Materials 12:3275

[52] Dos Santos DF, Lovisa LX, Santiago AAG, Siu Li M, Longo E, Bomio MRD, Motta FV (2020) Growth mechanism and vibrational and optical properties of SrMoO4: Tb3+, Sm3+ particles: green– orange tunable color. J Mater Sci 55:8610

[53] Meza-Rocha AN, Bordignon S, Speghini A, Caldino U, Huerta EF, Soriano-Romero O (2020) Lithium-aluminum-zinc phosphate glasses activated with Sm^{3+}, Sm^{3+} /Eu^{3+} and Sm^{3+}/Tb^{3+} for reddish-orange and white light generation. J Alloy Compd 846:156332

[54] Smet PF, Parmentier AB, Poelman D (2011) Selecting conversion phosphors for white lightemittingdiodes. J Electrochem Soc 158:R37–R54

[55] Katelnikovas A, Winkler H, Kareiva A, Jüstel T (2011) Synthesis and optical properties of green to orange tunable garnet phosphors for pcLEDs. Opt Mater 33:992–995

[56] Liu X, Li L, Noh HM, Moon BK, Choi BC, Jeong JH (2014) Chemical bond properties and charge transfer bands of O^{2-}–Eu^{3+}, O^{2-}–Mo^{6+} and O^{2-}–W^{6+} in Eu^{3+}-doped garnet hosts $Ln_3M_5O_{12}$ and ABO_4 molybdate and tungstate phosphors. Dalton Trans 43:8814–8825